Amorphization and evolution of magnetic properties during mechanical alloying of $Co_{62}Nb_6Zr_2B_{30}$: dependence on starting boron microstructure.

L.M. Moreno, J.S. Blázquez, J.J. Ipus, A. Conde.

Dpto. Física de la Materia Condensada, ICMSE-CSIC, Universidad de Sevilla, P.O. Box 1065, 41080 Sevilla, Spain.

Abstract

$Co_{62}Nb_6Zr_2B_{30}$ composition was mechanically alloyed using three different types of boron powders in the starting mixture: crystalline ϐ-B, commercial amorphous B and optimized amorphous B via ball milling. Using optimized amorphous B, amorphization process of the alloy is more efficient but milling to optimize amorphous B introduces some iron contamination. Boron inclusions (100-150 nm in size) remain even after long milling times. However, using amorphous boron reduces the fraction of boron distributed as inclusions to ~40% of the total B. Thermal stability at the end of the milling process is affected by the initial boron microstructure. Coercivity is reduced a half using amorphous B instead of crystalline B in the starting mixture.

1. Introduction

Amorphous materials present different properties from their crystalline counterparts due to the absence of translational symmetry. However, they have short range order (< 10 Å) and some authors propose the existence in some cases of the so-called medium range order (10-30 Å) [1]. Therefore, the characteristic microstructural length in these materials is of the order of the atomic distances and thus comparable to the characteristic lengths of different phenomena (e.g. exchange length for magnetic phenomena). This feature makes these materials attractive for both fundamental research and technological applications [2].

Co-based amorphous alloys have been studied due to their excellent soft magnetic properties at high temperatures and its good glass forming ability [3,4]. Conventional ways to produce these amorphous systems are rapid quenching (RQ) techniques, based on the original experiment of Paul Duwez [5]. In the decade of 80ôs of the last century, mechanical alloying (MA) was presented as an effective alternative to produce amorphous alloys [6], including soft magnetic amorphous/nanocrystalline alloys [7]. This powder processing technique starts from a heterogeneous mixture of elemental powders or compounds different from the final composition and leads to the formation of a homogeneous alloy. Fracture and cold welding phenomena are the processes driving this homogenization. MA or mechanical grinding (without net material transfer between the powders) are also effective to produce other metastable microstructures such as nanocrystalline, supersaturated solid solutions, quasicrystalline etc. [8].

A wide variety of amorphous alloy compositions contains boron as a glass forming element and amorphous structure stabilizer [9]. However, incorporation of boron atoms to the alloy matrix is not straightforward and boron inclusions have been observed even after long milling times [10,11,12]. This fact implies changes in the composition of the amorphous phase with respect to the nominal one and thus in the properties of the material.

Therefore, it is important to quantify the amount of B incorporated into the amorphous phase developed by MA. One of the reasons that difficult B incorporation in the amorphous matrix is the high hardness of the ß-B phase (33.5 GPa [13]). Therefore, other microstructures of the initial B could reduce this obstacle.

In this study, $Co_{62}Nb_6Zr_2B_{30}$ amorphous alloy was prepared by MA from a mixture of pure elemental powders. In order to enhance the boron incorporation into the amorphous matrix, samples were prepared using different boron microstructures and the effects of milling on the magnetic properties and the microstructure are studied.

2. Experimental

Ball milling experiments were performed in a planetary mill Fritsch Pulverisette 4 Vario. The ball to powder ratio was 10:1, the rotational speed of the main disk was 350 rpm and that of the vials was 700 rpm in opposite direction. A mass of 5 g of $Co_{62}Nb_6Zr_2B_{30}$ composition was prepared from elemental powders (Ó99% purity for the metals), with particle size d<70 µm for Co and Nb and d<150 µm for Zr. Two commercial boron powders were used: crystalline ß-boron (Ó99% purity) and amorphous boron (Ó96% purity). As commercial amorphous only shows ~50 % of amorphous phase [11], the amorphous fraction was increased by mechanical grinding (50 h using the same milling parameters) of this commercial amorphous boron. In the following, samples will be named referring to the boron type used as: cryst-B, am^{com}-B and am^{opt}-B, for the alloys using crystalline, commercial amorphous and optimized amorphous boron, respectively. Figure 1 shows the X-ray diffraction (XRD) patterns (using Cu KŬ radiation in a Bruker D8I diffractometer) of the boron powders used in the different starting mixtures. In the XRD pattern shown in Fig.1 for the optimized amorphous boron, the (110) diffraction maximum of the Ŭ-Fe phase appears due to contamination from the milling media.

After milling $Co_{62}Nb_6Zr_2B_{30}$ samples for times of 1, 2, 3, 5, 10, 20 and 40 h, some powder (~0.3 g) was taken out from the vials to characterize its morphology, composition,

microstructural evolution and thermal stability. The opening and closing of the vials were done under argon atmosphere in a Saffron Omega glove box to avoid oxygen and humidity contamination. For cryst-B alloy after 2 h milling, no free powder could be collected as the sample was coating the vial walls and balls forming a shiny surface.

Particle size distribution and morphology were studied by scanning electron microscopy (SEM) using secondary electron (SE) and backscattered electron (BSE) images in a Jeol JSM-6460 LV operated at 20 kV. Compositional evolution and partitioning were studied by energy dispersive X-ray (EDX) spectrocopy using an Incax-sight of Oxford Instruments taken stationary spots at the center of each probed particle. Thermal stability of the samples was studied using differential scanning calorimetry (DSC) in a Perkin-Elmer DSC7 under Ar flow. Magnetic properties were studied using a Lakeshore 7407 vibrating sample magnetometer (VSM) using a maximum applied magnetic ýeld H=1.5 T. Curie temperatures, T_C, were measured as the inflexion point of the temperature dependence of spontaneous specific magnetization, $\sigma_S(T)$, curves.

3. Results

3.1. Morphology and composition

The particle size after different milling times was obtained by averaging over a minimum of 100 particles for each sample. At short milling times (t<5 h) the powder particles were irregular in shape and with a broad size distribution, meanwhile at longer milling times (t>5h) the powder particles were almost spherical and with a narrow size distribution. SE images also show the existence of agglomerates since early milling times (t=3 or 5 h). These agglomerates were present in all samples but, for cryst-B alloy, the size of particles is larger and their number of particles per agglomerate is smaller than for samples prepared using amorphous boron. For example, cryst-B alloy after 40 h milling shows few hundreds particles per agglomerate, meanwhile am^{com}-B and am^{opt}-B alloys show thousand of particles per agglomerate. Figure 2 shows SE images distinguishing

between a large powder particle (3 h) and an agglomerate (5 h) for am^{com}-B alloy. Table 1 collects the data of powder and agglomerate sizes as well as the number of particles per agglomerate for each studied sample. To calculate the number of particles per agglomerate we have used the approximation that both powder particle and agglomerate are spherical, so the number of particles per agglomerate is proportional to the ratio between the agglomerate and particle mean volumes. Particle size decreases with milling, finally achieving sizes about 10 μm after 40 h milling. For agglomerates, there is not a clear tendency and their sizes are 100-200 μm for the three alloys.

BSE experiments supply compositional information of the surface of the powders. Figure 3 shows BSE images of the three studied alloys after selected milling times, where dark spots correspond to boron inclusions. This is confirmed by EDX results, where a qualitative enhancement of $K_{\breve{U}}$ line of B at 0.18 eV is observed (particularly for short milling times when B inclusions are larger, see inset in figure 3). Table 1 also collects the size of these boron inclusions, which decreases with milling time for the three alloys. Although, after 1 h milling, cryst-B sample shows bigger inclusions (about 400 nm) than those found for am^{com}-B and am^{opt}-B samples (about 200 nm), their sizes become similar after 10 h milling. However, number density of inclusions is bigger for cryst-B alloy than for the other ones. This fact remarks the difficulties to incorporate boron into the amorphous matrix. Number density and size of inclusions decreases with milling so, as milling progresses, boron is slowly incorporated into the amorphous matrix, although faster for alloys produced using amorphous boron.

EDX analysis performed at different points on the surfaces of the powders supply complementary information to BSE experiments. As milling progresses, compositional homogeneity increases in the three alloys. Moreover, presence of iron due to contamination from milling media is detected. Contamination increases in all samples with milling time, as shown in table 1 (data from averaging a minimum of five EDX spectra). At short milling times (1 and 2 h) iron distribution is highly heterogeneous and large fluctuations appear in

the Fe content and, for these times, table 1 shows the minimum and maximum Fe content found to give an idea of the dispersion of Fe content in the samples. For longer milling times, the iron content is homogenized (tÓ3 h). After 40 h milling am^{com}-B is the less contaminated sample (around 4 at. % of Fe, assuming the nominal value of 30 at.% of B in the sample), meanwhile cryst-B is much more contaminated (14 at.% of Fe). For am^{opt}-B, a value of 8 at.% of Fe is obtained. If we compare the evolution of Fe content for both alloys produced using amorphous boron, their difference should be related with the initial Fe contamination present in the optimized amorphous boron powder used in the starting mixture of am^{opt}-B. In fact, this difference increases as milling progresses and a value of ~1 at.% can be extrapolated for 0 h milling (using values for tÓ3 h milling to avoid heterogeneities found at lower milling times). This 1 at.% of Fe in the starting am^{opt}-B mixture must come from the contamination suffered by pure boron after 50 h milling, which after a simple calculation can be estimated as ~5 at.% of Fe in this B powder. This value is of the order of the obtained one after comparing the first halo and the (110) maximum of figure 1c and taken into account the different scattering factors of Fe and B atoms (~2 at.% of Fe).

3.2. Microstructure

For short milling times, XRD patterns of the three studied alloys show the lines of the hcp Co (002) at 2***d*** =44.4°, (101) at 2***d*** =47.2° and (2-10) at 2d =75.8° and bcc Nb (110) at 2d=38.5° and (211) at 2***d*** =69.5°. The small amount of Zr and the low scattering factor of B prevent the detection of their corresponding diffraction lines (or haloes). As milling progresses, intensity of crystalline peaks decreases and they even disappear, whereas an amorphous halo progressively becomes the main feature in the XRD patterns. In order to estimate phase fractions, crystalline size and microstrains, a deconvolution procedure of the amorphous halo and the overlapped crystalline peaks was performed. The amorphous fraction was estimated as the area ratio between this amorphous halo and the sum of crystalline and amorphous contributions. Crystal size and microstrains were estimated from

the width of the (002) line of the hcp Co. Amorphous fraction increases most effectively with milling for am^{opt}-B alloy among the studied alloys, reaching ~100% of amorphous fraction after 10 h milling. On the other hand, cryst-B alloy recrystallizes after 40 h milling, meanwhile for the samples produced using amorphous boron, recrystallization is not observed for the explored milling times. Crystal sizes of the remaining hcp Co phase reduces below 5 nm after 10 h milling and the microstrains increase to ~0.3%. Values obtained for amorphous fraction, crystal size and microstrains are shown in table 1.

3.3. Thermal stability

Figure 4 shows the DSC scans of the samples after 40 h milling, for different heating rates. For cryst-B alloy DSC curves show three transformation processes (peak temperatures, T_p, about 700 K, 930 K and 990 K, respectively), for am^{com}-B two transformations appear (T_p about 700 K and 930 K, respectively) and for am^{opt}-B four transformations appear (T_p about 670 K, 880 K, 920 K and 940 K, respectively). These transformations can be associated to different phenomena, as relaxation, crystallization and any other stabilization process. Kissinger method [14] was used to calculate the activation energies, Q, for the different transformations. This method uses a linear relationship between $\ln(\beta/T_P^2)$ and T_p^{-1}, where β is the hating rate. Table 2 collects the resulting activation energies. For those cases, for which transformations are overlapped, Gaussian fittings were used to estimate T_p. The values of Q~1 eV points to relaxation phenomena, whereas higher Q values should correspond to crystallization processes. For the melt spun ribbons, DSC scan shows a single crystallization process at 950 K with Q=5.2 eV in our explored temperature range and relaxation phenomena are much less significant than for mechanically alloyed samples [4].

3.4 Magnetic properties

Figure 5 shows the data of coercive field, H_C, and spontaneous specific magnetization, σ_S, after selected milling times for the three studied alloys. We observe a

continuous decrease for both magnitudes with milling time. During milling, H_C decreases from Ó120 Oe, to 25 Oe for cryst-B, 13 Oe for am^{opt}-B and 10 Oe for am^{com}-B, after 40 h milling. Therefore, the use of amorphous boron (commercial or optimized) reduces to a half the coercive field with respect to the alloy prepared using crystalline boron. The values of σ_S were estimated extrapolating to zero field a linear fit to the $\sigma(H)$ values for fields between 1.2 T and 1.5 T. After 40 h milling, the lowest spontaneous magnetization value was found for am^{com}-B alloy. A higher crystalline fraction for cryst-B alloy and a higher Fe contamination in am^{opt}-B alloy could explain this fact.

4. Discussion

In order to study the microstructural evolution corresponding to the different DSC events observed, samples of am^{com}-B alloy after 40 h of milling were heated up to 823 K and 973 K, above the two well resolved peak temperatures that appear in the DSC scan (see Fig. 4). Figure 6 shows the XRD patterns of these thermally treated samples, showing that the first DSC transition corresponds to relaxation phenomena because no crystallization was detected, whereas the second DSC transition corresponds to the crystallization of a single fcc $Co_{21}Nb(Zr)_2B_6$ intermetallic phase (with a lattice parameter a=10.53 Å) and disappearance of amorphous phase. This result disagrees with the crystallization of amorphous melt-spun ribbons of the same composition [4], where, besides this fcc phase, other boride phases (richer in boron) were found. This could be related to the presence of boron inclusions in our studied alloy. The amount of boron incorporated into the amorphous matrix can be estimated from the fact that no boron rich phases are formed in the MA sample. Assuming that the metal to B compositional ratio of the amorphous phase and that of the single product $Co_{21}(Nb,Zr)_2B_6$ phase are the same, the approximate composition of the amorphous matrix should be $(Co_{62}Nb_6Zr_2)_{79.5}B_{20.5}$. This indicates that only about 60% of the initial boron was effectively incorporated into the matrix, whereas about 40% remains as inclusions.

Another way to estimate the boron content can be based on the high value of the amorphous Curie temperature, T_C, with respect to that of a melt-spun sample (550 and 210 K, respectively). From literature data of $Co_{100-X}B_X$ alloys [9], T_C decreases about 30 K per atomic percent of boron. Therefore, an approximate composition of the amorphous matrix should be $(Co_{62}Nb_6Zr_2)_{81}B_{19}$, which is in good agreement with our previous estimation. Moreover, the presence of Fe due to contamination in the milled sample, should also lead to an enhancement of T_C of the amorphous phase.

The continuous decrease of σ_S as milling progresses is related to the progressive amorphization of the sample. In fact, as shown in figure 7 (a), σ_S decreases as X_C decreases due to the smaller specific magnetization of the amorphous phase with respect to the crystalline one.

The evolution of coercivity with milling is also ascribed to the microstructural evolution of the samples and could be understood through the analysis of the effective magnetic anisotropy, $K_{eff}=M_S H_C/p_C$, where M_S is the spontaneous magnetization calculated from σ_S assuming a density of 8 g/cm^3 and p_C is a geometrical factor close to unity. Evolution of K_{eff} during milling is separated in two regimes [15]. At short milling times, K_{eff} increases dominated by the fast increase of microstrains (as observed for different mechanically alloyed powders [16,17]). However, for long milling times, a decrease in K_{eff} is observed, ascribed to refinement of crystals. In the present results, the short milling time regime is not observed and must correspond to milling times below one hour. In the second regime, K_{eff} can be described as the addition of a long range magnetoelastic contribution in the scale of the powder particles and two averaged short range contributions (magnetoelastic and magnetocrystalline ones) in the scale of the nanocrystals [15]. Taking into account the presence of amorphous phase, an implicit expression for K_{eff} is:

$$K_{eff} = \sqrt{{K_{u,ma}}^2 + \left({K_{u,mi}}^2 + {X_C}^2 {K_1}^2\right)\frac{{D_{Co}}^3 {K_{eff}}^{3/2}}{A^{3/2}}} \qquad (1)$$

J

Where $K_{u,ma}$ and $K_{u,mi}$ are the long and short range magnetoelastic anisotropy, respectively; K_1 is the magnetocrystalline anisotropy of hcp Co, D_{Co} is the average crystal size and A is the exchange stiffness constant.

Figure 7 (b) shows K_{eff}^2 vs $X_C^2 D_{Co}^3 K_{eff}^{3/2}$ for milling times long enough to consider saturated microstrains. Using $A \sim 10^{-11}$ J/m and neglecting $K_{u,mi}$ with respect to K_1, the slope of the linear fit leads to values of K_1 between 0.6 MJ/m^3 for cryst-B alloy and 2 MJ/m^3 for the alloys produced using amorphous boron. The value of $K_{u,ma} \sim$3-4 kJ/m^3 estimated from the intercept supports our previous approximation neglecting $K_{u,mi}$ with respect K_1. The points corresponding to low milling times have been neglected because the microstrains were not constant. These values of magnetocrystalline anisotropy are of the same order than that of hcp Co [18].

5. Conclusions

An amorphous phase from a starting mixture with nominal composition $Co_{62}Nb_6Zr_2B_{30}$ was successfully produced by mechanical alloying using different types of boron powders in the starting mixtures: crystalline ɓ-B, commercial amorphous boron (about 50% amorphous phase) and optimized amorphous boron by ball milling (with approximately 5 at.% of Fe from contamination). However, remaining B inclusions imply that the composition of the amorphous phase differs from the nominal value. The main conclusions derived from this study are listed below:

- Using optimized amorphous boron the amorphization occurs for shorter milling times than using the commercial crystalline or amorphous powders.
- Boron inclusions are observed in all studied samples even at the end of the milling process but the use of amorphous boron in the initial mixture reduces the number of inclusions, decreasing the inhomogeneity of the alloy.

- Boron is more effectively introduced into the matrix (approximately 60% of the total B) when amorphous boron powder is used in the starting mixture.
- The use of crystalline B yields higher iron content from contamination.
- Crystallizaton of amorphous phase occurs above 800 K, whereas relaxation phenomena appear below this temperature (less significant for the sample produced using optimized amorphous B).
- Spontaneous magnetization reduces as crystalline fraction reduces.
- Coercivity of samples milled 40 h is reduced 50% using amorphous B in the initial mixture with respect to samples prepared using crystalline B.
- The evolution of the effective magnetic anisotropy can be explained from two contributions: long range magnetoelastic and short range averaged magnetoelastic and magnetocrystalline. The magnetoelastic contribution is negligible with respect to magnetocrystalline one.

Acknowledgements:

This work was supported by the Spanish Ministry of Science and Innovation (MICINN) and EU FEDER (project MAT2010-20537), the PAI of the Regional Government of Andalucía (RGA) (project P10-FQM-6462). L.M. Moreno acknowledges a research internship funded by the Spanish Ministry of Education. J.J. Ipus acknowledges a research fellowship from RGA.

Tables

Table 1

Alloy	t (h)	d (μm)	d_{Agg} (±10 μm)	N (±30%)	D_{Incl} (±10 nm)	Fe content (at.%)	X_{Am} (±5 %)	D_{Co} (±1.0 nm)	$\mathring{U}_{Co}$ (%)
cryst-B	1	228±10			460	1.1 (0-4.0)	0	9.5	0.2
	3	111±10			199	3.2±0.6	74	5.3	0.3
	5	78±10			204	4.6±1.6	80	5.3	0.3
	10	26±5	172	310	157	8.0±0.5	84	4.0	0.4
	20	25±1	125	3	157	10.8±0.5	100		
	40	21±1	153	390	154	13.6±1.3	87	7.5	0.2
am^{com}-B	1	144±10			199	1.4 (0-8.4)	46	10.0	0.1
	2	76±10			194	0.1 (0-0.4)	55	7.3	0.2
	3	54±10			183	0.5±0.3	83	4.0	0.4
	5	21±2	226	1200	188	0.6±0.5	88	4.0	0.4
	10	16±1	156	900	166	2.7±0.9	89	4.4	0.3
	20	12±1	150	1800	135	3.3±0.2	94	4.3	0.4
	40	7.8±0.5	237	28000	114	3.6±0.4	91	3.9	0.4
am^{opt}-B	1	239±10			197	2.1 (0-17.6)	67	13.5	0.1
	2	109±10			191	2.0 (1.2-3.4)	77	8.9	0.2
	3	112±10			183	1.1±0.3	81	7.9	0.2
	5	20±2	133	280	178	1.9±0.5	91	3.9	0.4
	10	23±1	111	120	160	4.7±0.3	100		
	20	18±2	239	2400	145	6.0±0.5	100		
	40	10±1	162	4900	140	7.9±0.8	100		

Table 1. Powder particle size (d), agglomerate size (d_{Agg}), number of particles per agglomerate (N), size of boron inclusions (D_{Incl}), iron content assuming 30 at.% B (the lowest and highest values appear in parenthesis), crystal size (D_{Co}) and microstrains ($\mathring{U}_{Co}$) of remaining hcp Co and amorphous fraction (X_{Am}) for the three studied alloys after selected milling times (t).

Table 2

Transformation	Q (eV)			
	cryst-B	am^{com}-B	am^{opt}-B	Melt spun [4]
T1	1.7±0.2	1.6±0.1	1.1±0.2	
T2		3.7±0.6	2.3±0.3	
T3	6.0±0.7		6.8±0.6	5.2±0.2
T4	6.6±0.7		6.2±0.3	

Table 2. Activation energies calculated by Kissinger method.

Figure captions

Figure 1. XRD patterns of boron powders used in the starting mixtures.

Figure 2. SEM images (SE mode) of samples of am^{com}-B after 3 (upper frames) and 5 (lower frames) hours of milling, respectively. Dotted rectangles mark the corresponding magnified views at insets.

Figure 3. SEM images (BSE mode) for the three studied alloys after selected milling times. The inset shows an EDX spot analysis of the corresponding region encircled in the image.

Figure 4. DSC scans for the three studied alloys after 40h milling at different heating rates. Ti indicates the transformation as labeled in table 2. The inset shows an enlarged view of the high temperature range for T4 of cryst-B sample.

Figure 5. Coercive field and spontaneous specific magnetization at room temperature after selected milling times. Hollow symbols correspond to the data of the recrystallized cryst-B sample.

Figure 6. XRD patterns for am^{com}-B alloy after 40 h milling at room temperature and heated up to 823 K and 973 K. The different indexed maxima correspond to fcc $Co_{21}(Nb,Zr)_2B_6$ phase.

Figure 7. Data of spontaneous specific magnetization vs crystalline fraction (a) and plot of K_{eff}^2 vs $K_{eff}^{3/2}X_C^2D_{Co}^3$ (b) following equation (1) for the three studied alloys. Lines represent the linear fitting to the data.

Figure 1

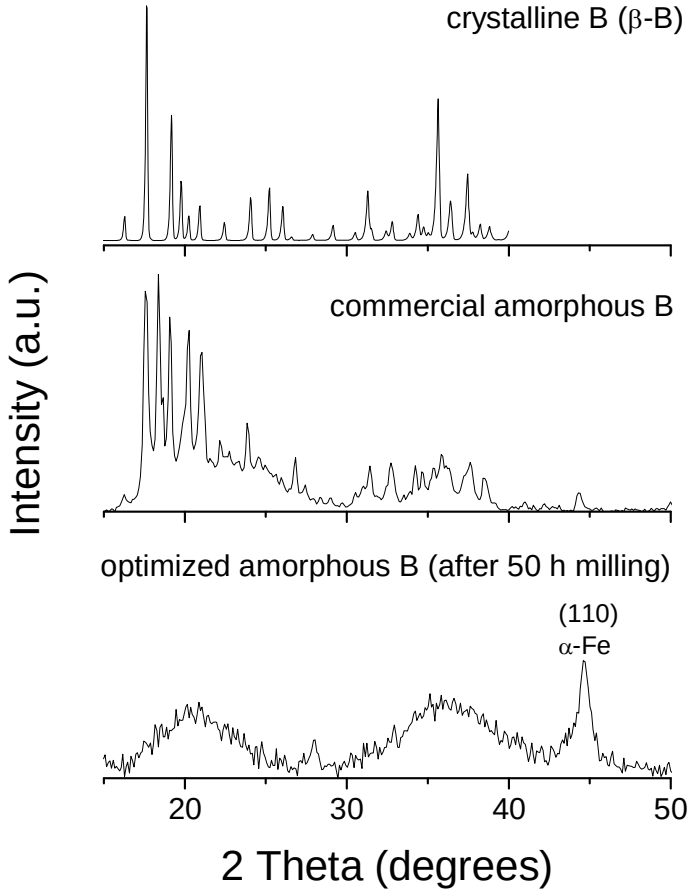
crystalline B (β-B)
commercial amorphous B
optimized amorphous B (after 50 h milling)
(110)
α-Fe
Intensity (a.u.)
20
30
40
50
2 Theta (degrees)

Figure 2

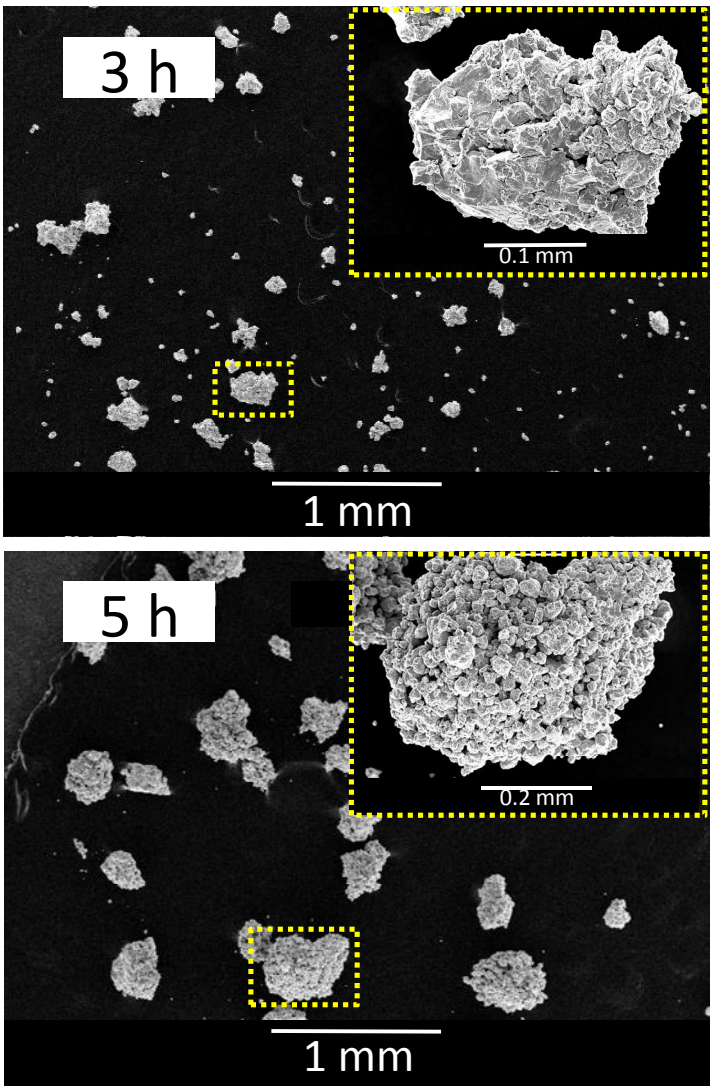

Figure 3

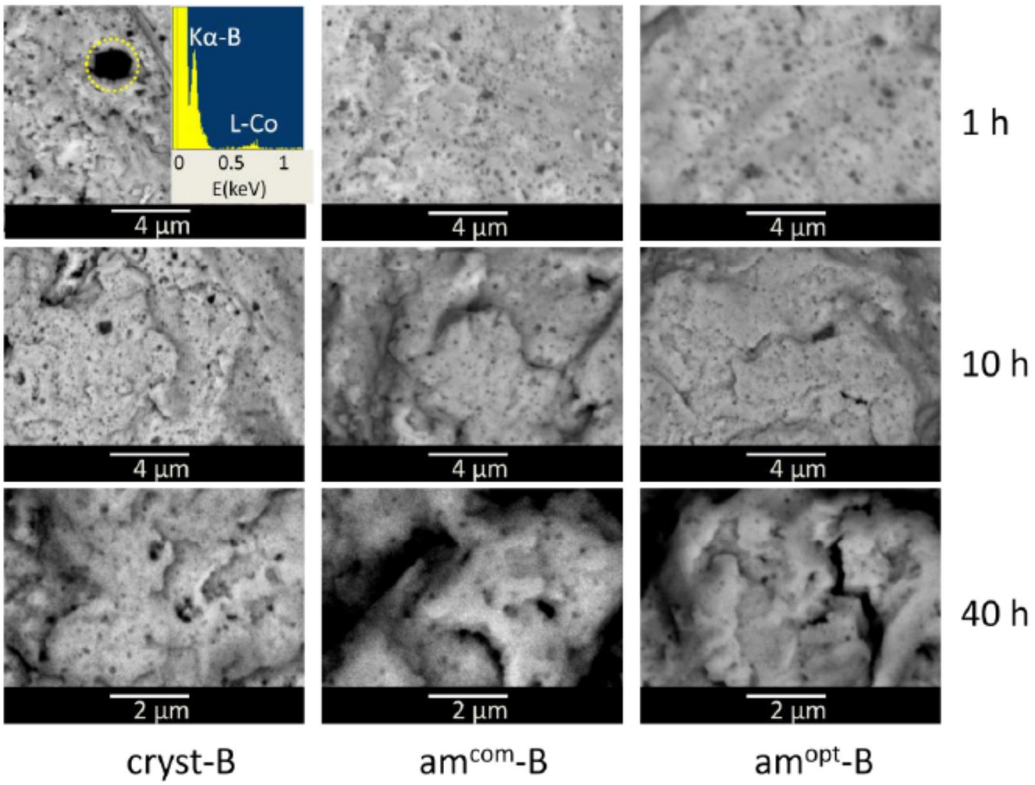
Kα-B
L-Co
0 0.5 1
E(keV)
4 µm
4 µm
4 µm
1 h
4 µm
4 µm
4 µm
10 h
2 µm
2 µm
2 µm
40 h
cryst-B
am^com-B
am^opt-B

Figure 4

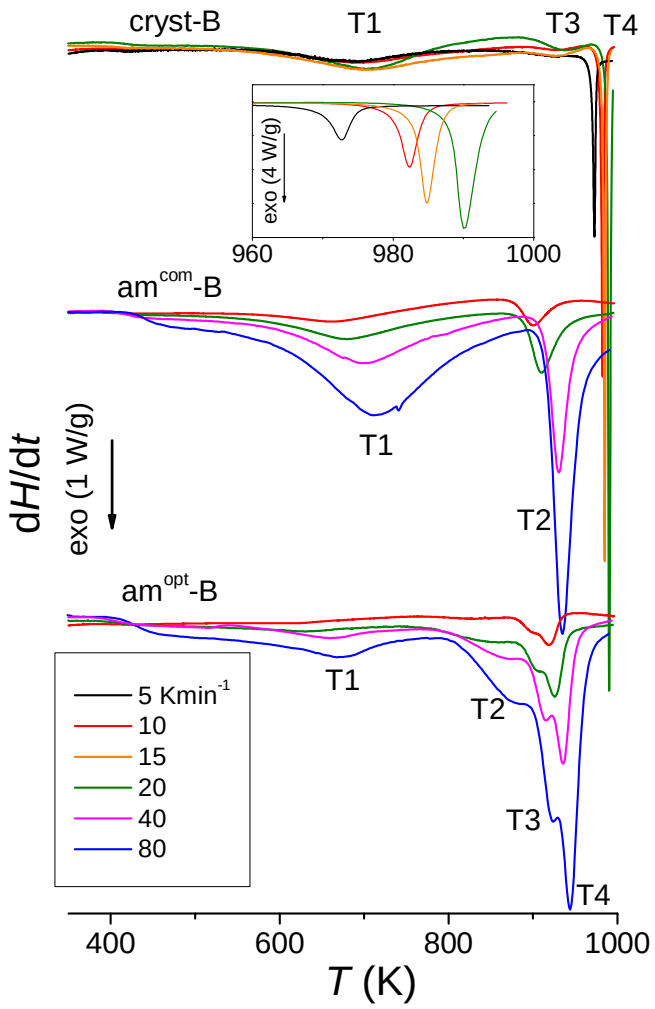
cryst-B
T1
T3
T4
exo (4 W/g)
960
980
1000
am^com-B
T1
T2
dH/dt
exo (1 W/g)
am^opt-B
T1
T2
T3
T4
5 Kmin^-1
10
15
20
40
80
400
600
800
1000
T (K)

Figure 5

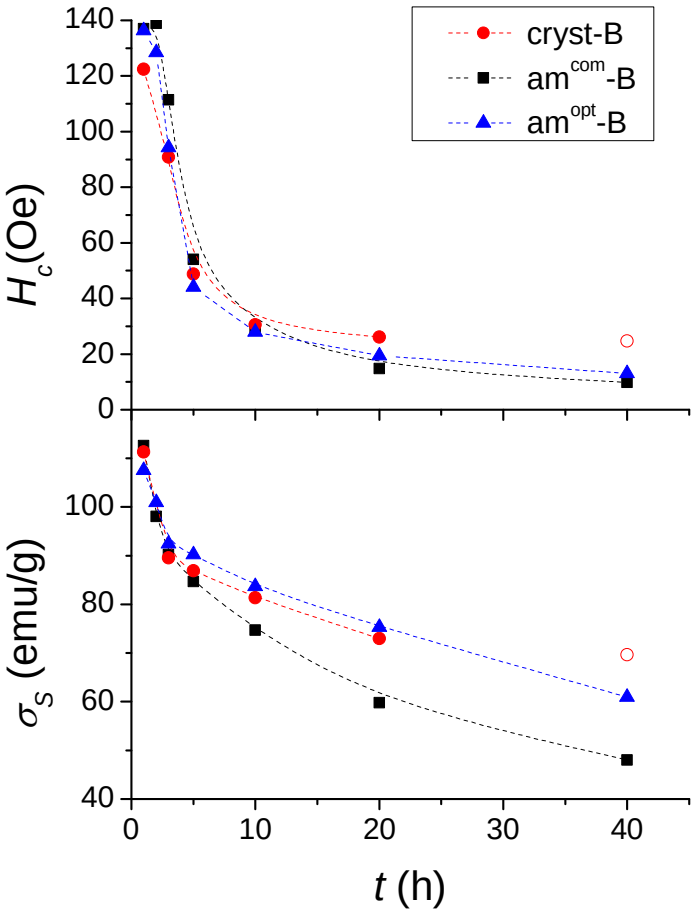

Figure 6

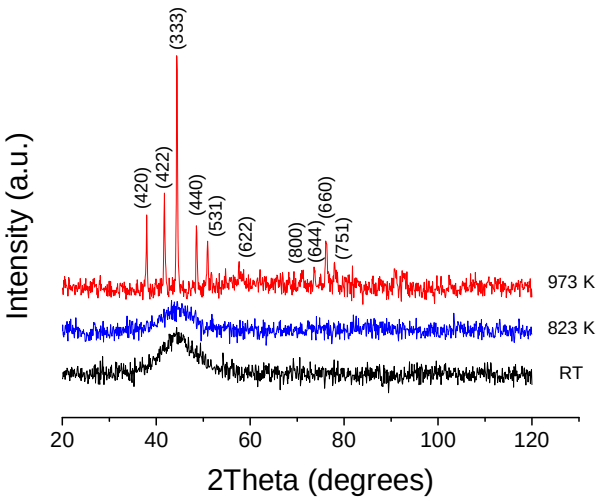

Figure 7

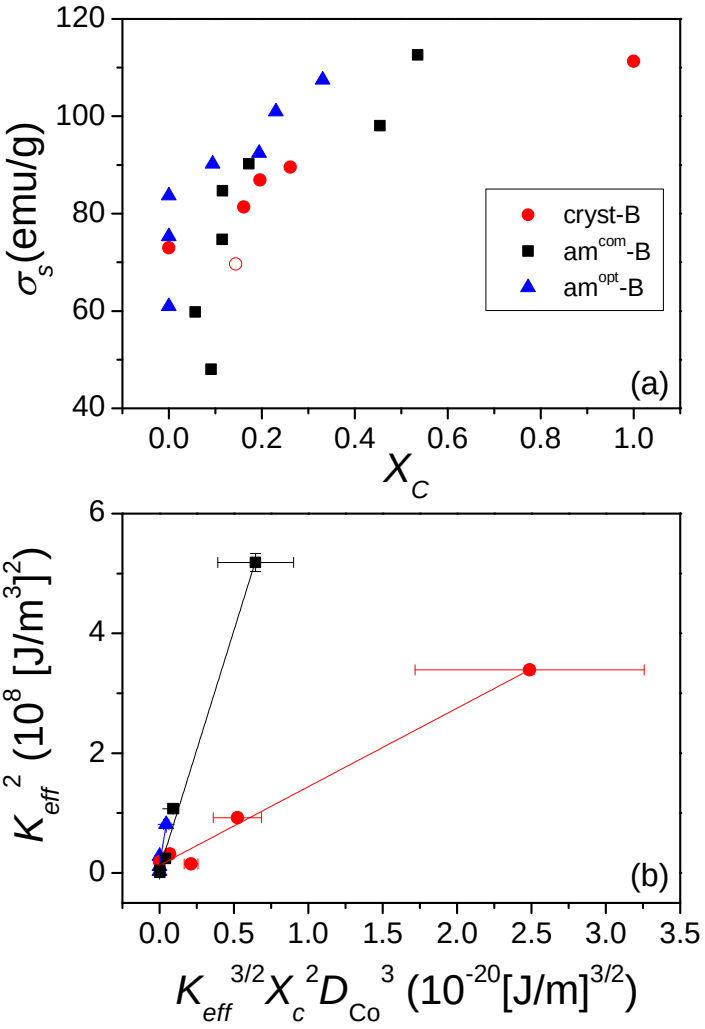
120
100
80
60
40
σ_s(emu/g)
cryst-B
am^{com}-B
am^{opt}-B
(a)
0.0
0.2
0.4
0.6
0.8
1.0
X_C
6
4
2
0
K_{eff}^{2} (10^{8} [J/m^{3}]^{2})
(b)
0.0
0.5
1.0
1.5
2.0
2.5
3.0
3.5
$K_{eff}^{3/2} X_c^{2} D_{Co}^{3}$ (10^{-20}[J/m]$^{3/2}$)

J

References

[1] G. Li, K. B. Borisenko, Y. Chen, D. Nguyen-Manh, E. Ma, D. J. H. Cockayne, Acta Mater. 57 (2009) 804-811.
[2] M. E. McHenry, M. A. Willard, D. E. Laughlin, Prog. Mater. Sci. 44 (1999) 291-433.
[3] A. Inoue, B. L. Shen, A. Takeuchi, Mater. Sci. Eng. A 441 (2006) 18-25.
[4] J. M. Borrego, C. F. Conde, A. Conde, S. Roth, H. Grahl, A. Ostwald, and J. Eckert, J. Appl. Phys. 92 (2002) 6607-6611.
[5] W. Klement, R. H. Willens, P. Duwez, Nature 187 (1960) 869-870.
[6] Benjamin JS. In: Arzt E, Schultz L, editors. New materials by mechanical alloying techniques. Oberursel, Germany: DGM Informationgesellschaft, 1989. pp. 3-18.
[7] J. S. Blázquez, J. J. Ipus, S. Lozano-Pérez, A. Conde, JOM 65 (2013) 870-882.
[8] C. Suryanarayana. Prog. Mater. Sci 46 (2001) 1-184.
[9] H. P. J. Wijn, Landolt-Börnstein, Neue serie: Magnetische Eigenschaften von Metallen, Springer-Verlag, Berlin-Heidelberg, 1991. P.126.
[10] J. J. Ipus, J. S. Blázquez, S. Lozano-Pérez, A. Conde, Phil. Mag. 89 (2009) 1415-1423.
[11] J. J. Ipus, J. S. Blázquez, V. Franco, S. Lozano-Pérez, A. Conde, J. All. Compd. 553 (2013) 119-124.
[12] M. Krasnowski, A. Antolak-Dudka, T. Kulik, Intermetallics 19 (2011) 1243-1249.
[13] J. O. Carlsson, T. Lundström, J. Less-Common Met. 22 (1970) 317-320.
[14] J. M. Criado, A. Ortega, J. Non-Cryst. Solids 87 (1986) 302-311.
[15] T. D. Shen, R. B. Schwarz, J. D. Thompson, Phys. Rev. B 72 (2005) 014431.
[16] J. J. Ipus, J. S. Blázquez, V. Franco, C. F. Conde, A. Conde, J. All. Compd. 509 (2011) 1407-1410.
[17] J. J. Ipus, J. S. Blázquez, V. Franco, A. Conde, S. Lozano-Pérez, Phys. Express 2 (2012) 8.
[18] Bonnenberg, Hempel, Wijn in Springer Materials, The Landolt-Börnstein Database, Landolt-Bornstein New Series III/19a p. 274.